









## Article

# Synthesis of Nitrogen-Doped Biomass-Based Activated-Carbon-Supported Nickel Nanoparticles for Hydrazine Oxidation

Virginija Ulevičienė<sup>1</sup>, Aldona Balčiūnaitė<sup>1</sup> , Daina Upskuvienė<sup>1</sup>, Ance Plavniece<sup>2</sup> , Aleksandrs Volperts<sup>2</sup> , Galina Dobeļe<sup>2</sup> , Aivars Zhurīnsh<sup>2</sup> , Gediminas Niaura<sup>1</sup> , Loreta Tamašauskaitė-Tamašiūnaitė<sup>1,\*</sup> , and Eugenijus Norkus<sup>1</sup> 

<sup>1</sup> Center for Physical Sciences and Technology (FTMC), Sauletekio Ave. 3, LT-10257 Vilnius, Lithuania; virginija.uleviciene@ftmc.lt (V.U.); aldona.balciunaite@ftmc.lt (A.B.); daina.upskuviene@ftmc.lt (D.U.); gediminas.niaura@ftmc.lt (G.N.); eugenijus.norkus@ftmc.lt (E.N.)

<sup>2</sup> Latvian State Institute of Wood Chemistry, Dzerbenes Str. 27, LV-1006 Riga, Latvia; ance.plavniece@kki.lv (A.P.); aleksandrs.volperts@kki.lv (A.V.); galina.dobeļe@kki.lv (G.D.); aivarsz@edi.lv (A.Z.)

\* Correspondence: loreta.tamasauskaite@ftmc.lt

**Abstract:** In this study we present an application of wood biomass—alder wood char—as the carbon precursor for the synthesis of novel and sustainable nitrogen-doped activated-carbon-supported nickel nanoparticle catalyst (AWC-Ni-N) for hydrazine oxidation. For comparison, the wood-based carbon material doped with nitrogen only (AWC-N) was also synthesized. Extensive characterization, including SEM, Raman spectroscopy, XPS, and XRD revealed the catalysts' microstructure and properties. Electrochemical testing demonstrated that the AWC-Ni-N catalyst significantly enhanced the efficiency of the hydrazine oxidation reaction. In addition, direct N<sub>2</sub>H<sub>4</sub>-H<sub>2</sub>O<sub>2</sub> single-fuel-cell tests were conducted using the prepared AWC-N and AWC-Ni-N catalysts as the anodes and cathodes. Peak power densities of up to 10.8 mW cm<sup>−2</sup> were achieved at 25 °C, corresponding to a current density of 27 mA cm<sup>−2</sup> and a cell voltage of 0.4 V when the AWC-Ni-N catalyst was used as both the anode and cathode. Furthermore, the peak power density increased by approximately 1.6 and 2.9 times, respectively, when the operating temperature was raised from 25 °C to 55 °C for the AWC-N and AWC-Ni-N catalysts. Overall, the AWC-N and AWC-Ni-N catalysts demonstrated significant potential as anode and cathode materials in direct N<sub>2</sub>H<sub>4</sub>-H<sub>2</sub>O<sub>2</sub> fuel cells.

**Keywords:** biomass; nitrogen-doped carbon; nickel; hydrazine oxidation; fuel cells



Academic Editor: Sergio Nogales Delgado

Received: 9 March 2025

Revised: 16 April 2025

Accepted: 16 April 2025

Published: 19 April 2025

**Citation:** Ulevičienė, V.; Balčiūnaitė, A.; Upskuvienė, D.; Plavniece, A.; Volperts, A.; Dobeļe, G.; Zhurīnsh, A.; Niaura, G.; Tamašauskaitė-Tamašiūnaitė, L.; Norkus, E. Synthesis of

Nitrogen-Doped Biomass-Based Activated-Carbon-Supported Nickel Nanoparticles for Hydrazine Oxidation. *Catalysts* **2025**, *15*, 400. <https://doi.org/10.3390/catal15040400>

**Copyright:** © 2025 by the authors. Licensee MDPI, Basel, Switzerland. This article is an open access article distributed under the terms and conditions of the Creative Commons Attribution (CC BY) license (<https://creativecommons.org/licenses/by/4.0/>).

## 1. Introduction

Recently, there has been a growing interest in carbon-based catalysts due to their unique properties and sustainability. These catalysts are becoming increasingly attractive to various industries and researchers. Activated carbon and nanostructured carbon materials, such as graphene, doped carbon, and carbon nanotubes, have a large surface area. This enables them to adsorb reagents more efficiently and catalyze reactions effectively [1,2]. Carbon-based catalysts are versatile and can be used in electrochemical reactions, water purification, organic compound synthesis, and other processes. Since they are often produced from biomass or waste, they are both economically attractive and affordable, reducing dependence on expensive metals such as platinum or palladium. The

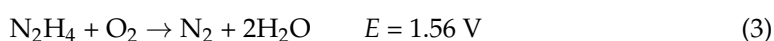
use of biomass waste for catalyst synthesis also contributes to waste reduction and supports the development of a circular economy [3,4].

Biomass is a popular carbon precursor in terms of its renewability, earth abundance, environmental friendliness, low cost, non-toxicity, sustainability, ease of production, and the variety of heteroatoms (N, P, S, etc.) in its intrinsic composition. In addition, biomass-derived carbons have emerged as a promising potential alternative to the carbon-based catalysts that are conventionally produced. They hold great promise as a renewable source of sustainable carbon materials for the next generation of energy storage and conversion systems. Carbon can be doped with nitrogen, sulfur, or metals, or it can be treated with chemicals. This makes it more active, conductive, and selective. For instance, the nitrogen doping of carbon materials has been shown to improve their electrical conductivity and reaction selectivity. Similarly, the incorporation of metal particles has been demonstrated to enable better control of reaction mechanisms [5–7]. Furthermore, nitrogen and metal (Ni, Co, Cu, Mo) doping creates a synergistic effect that is particularly important in electrocatalytic reactions, such as the hydrazine oxidation reaction (HzOR), by improving the reaction rate, selectivity, and energy efficiency. Nitrogen atoms are incorporated into the carbon lattice to form nitrogen-containing structures (e.g., pyridine or pyrrole). This increases the electron density on the catalyst surface, facilitating electron transfer during the reaction. Nitrogen doping generates more active sites on the catalyst surface, enabling easier adsorption of reactants such as hydrazine ( $\text{N}_2\text{H}_4$ ). It also modifies the catalyst's surface properties, making it more selective for the desired reaction and reducing the likelihood of side reactions [8–10]. On the other hand, metals (Ni, Co, Cu, Mo) also act as redox centers and assist in the HzOR. These metal centers can quickly switch between different oxidation states, allowing them to effectively facilitate redox reactions. Although doping with transition metals such as Co, Cu, and Mo can enhance catalytic properties, each metal has notable limitations. Cobalt-based catalysts often suffer from lower catalytic stability, higher operational voltages, and increased toxicity concerns, restricting their practical application in sustainable catalytic processes [11,12]. Although initially active, copper catalysts often experience rapid deactivation due to metal leaching, surface oxidation, and susceptibility to corrosion during prolonged electrochemical reactions [13]. Similarly, molybdenum-based catalysts pose challenges due to their relatively low intrinsic electrical conductivity and poor electrochemical stability, particularly in strongly alkaline media, which limit their effectiveness in long-term applications [14,15]. In contrast, nickel (Ni) emerges as a particularly viable alternative due to its superior electrochemical stability, high catalytic efficiency, relative abundance, low cost, and minimal environmental concerns compared with these metals. Moreover, nickel-based catalysts have demonstrated remarkable performance in terms of activity, durability, and resistance to corrosion under harsh operational conditions, such as those involving  $\text{NiFe}_2\text{O}_4$ -rGO composites, Ni-W alloys, and nickel iron sulphide/hydroxide catalysts [12,15–17]. These attributes make nickel highly attractive for sustainable catalytic applications, especially for crucial reactions such as the hydrazine oxidation reaction (HzOR) and related electrochemical processes [12,17]. In addition, nickel particles on the catalyst surface enhance the adsorption of  $\text{N}_2\text{H}_4$  molecules, stabilize intermediate states, and accelerate the reaction rate. The interaction between nitrogen doping and nickel atoms enhances the stability and efficiency of nickel during the reaction. Together, nitrogen and nickel reduce the activation energy of the reaction, enabling faster and more efficient processes. In addition, doping improves the chemical and structural stability of the catalyst, ensuring long-lasting catalytic activity. This makes nitrogen- and nickel-doped catalysts a cost-effective and sustainable alternative for various catalytic applications [18–22]. The use of nickel as the active metal allows the avoidance of more expensive noble metals, such as platinum, palladium, and ruthenium without com-

promising catalytic efficiency [23–25]. The importance of the HzOR lies in its applications in sustainable energy production, environmental solutions, and the development of advanced catalysts.  $\text{N}_2\text{H}_4$  serves as a fuel source in direct hydrazine fuel cells (DHFCs) [26,27], where its oxidation reaction enables efficient electricity generation with high energy density and low emissions. This makes it particularly relevant for powering vehicles and portable devices. The DHFC is based on the HzOR in an alkaline medium, which occurs at the anode (Equation (1)) and the reduction of oxygen ( $\text{O}_2$ ) at the cathode (Equation (2)):



The total cell reaction can be written as Equation (3) [28,29]:



The HzOR produces only  $\text{H}_2\text{O}$  and  $\text{N}_2$  as by-products (Equation (1)) [30,31]. From this point of view,  $\text{N}_2\text{H}_4$  can act as a carbon dioxide ( $\text{CO}_2$ ) reducer because its oxidation produces nitrogen and water without contributing to atmospheric  $\text{CO}_2$  levels. This property highlights its potential role in mitigating carbon emissions. The HzOR, a critical reaction in applications such as DHFCs, rocket fuels, and carbon-neutral energy systems, relies heavily on the development of advanced catalytic materials [32,33]. Moreover,  $\text{N}_2\text{H}_4$  as a fuel has many advantages, including its wide availability, a high theoretical potential of 1.56 V of DHFC—higher than many other fuels such as hydrogen (1.24 V) or methanol (1.19 V)—resulting in high power density, and the absence of the greenhouse gas  $\text{CO}_2$  or carbon-based intermediates that could poison the electrocatalyst [28,34,35]. Typically,  $\text{O}_2$  is used as the oxidant in fuel cells, but fuel cells using hydrogen peroxide ( $\text{H}_2\text{O}_2$ ) as the oxidant have also been proposed and are finding various potential applications [28,36–38]. The reduction of  $\text{H}_2\text{O}_2$  at the cathode in an acidic medium is given by Equation (4):



The theoretical cell voltage of 2.93 V of the direct hydrazine–hydrogen peroxide ( $\text{N}_2\text{H}_4$ - $\text{H}_2\text{O}_2$ ) fuel cell (Equation (5)) is significantly higher than that of the DHFC (1.56 V), which uses  $\text{O}_2$  as the oxidant.



The fact that  $\text{H}_2\text{O}_2$  is a liquid oxidant at ambient temperature and pressure makes it easier to transport, store, and handle than  $\text{O}_2$ . It has the additional advantage of being good to use in a small-volume single-stack fuel cell. The development of electrocatalysts with reasonable cost and high electroactivity for fuel oxidation is of industrial importance. In this study, we present the synthesis of novel nitrogen-doped biomass-based catalyst-supported nickel nanoparticles with the aim of improving HzOR efficiency while maintaining high activity and durability. The results highlight the novelty of biomass-derived catalysts in the advancement of green catalytic technologies and their potential for energy and environmental applications. In addition, this study introduces a novel sustainable catalyst, that provides a cost-effective alternative to noble metals. By enhancing the efficiency of the HzOR, it supports carbon-neutral energy systems and is consistent with green chemistry principles, demonstrating the relevance of addressing both environmental and energy challenges. The energy released during the HzOR can be harnessed for various energy systems, offering potentially higher efficiencies compared with traditional fuel sources. The

study of the HzOR provides valuable insights into the activity, selectivity, and durability of catalysts, which are key to optimizing the process.

## 2. Results

### 2.1. Microstructure and Morphology Studies

In this study, we propose a simple strategy for synthesizing an efficient non-noble metal-based carbon catalyst. The SEM images in Figure 1 illustrate the morphological differences between AWC-N (a) and AWC-Ni-N (b) catalysts at different magnifications. AWC-N (Figure 1a) had a highly porous structure with irregular, rough particles. At higher magnifications, micro- and mesopores were visible, along with sharp edges and a layered morphology, indicating effective chemical activation. In contrast, AWC-Ni-N (Figure 1b) exhibited more compact and interconnected particles. At higher magnifications (Figure 1b), wire-like or fibrous nanostructures were observed, likely due to the catalytic effect of nickel during the co-doping process. The wire-like or fibrous nanostructures observed in the AWC-Ni-N catalyst (Figure 1b, right panel) were absent in the AWC-N sample (Figure 1a), clearly indicating that their formation was linked to the incorporation of nickel during the synthesis process. Nickel has been widely reported to act as a catalyst for the growth of carbon nanofibers (CNFs) and carbon nanotubes (CNTs) under thermal conditions [39,40]. During the co-doping process, nickel likely facilitated the decomposition of carbon-containing precursors and promoted the precipitation of carbon into one-dimensional (1D) forms through a catalytic mechanism. Although no external carbon source was introduced, it is likely that carbonaceous species derived from the precursor material (e.g., biomass-derived alder wood char) underwent partial decomposition under thermal treatment in the presence of Ni, resulting in the formation of web-like fibrous carbon structures. Nitrogen co-doping may have further influenced the morphology by stabilizing these 1D structures. Such nanostructures improved the catalytic performance of AWC-Ni-N in subsequent electrochemical measurements.

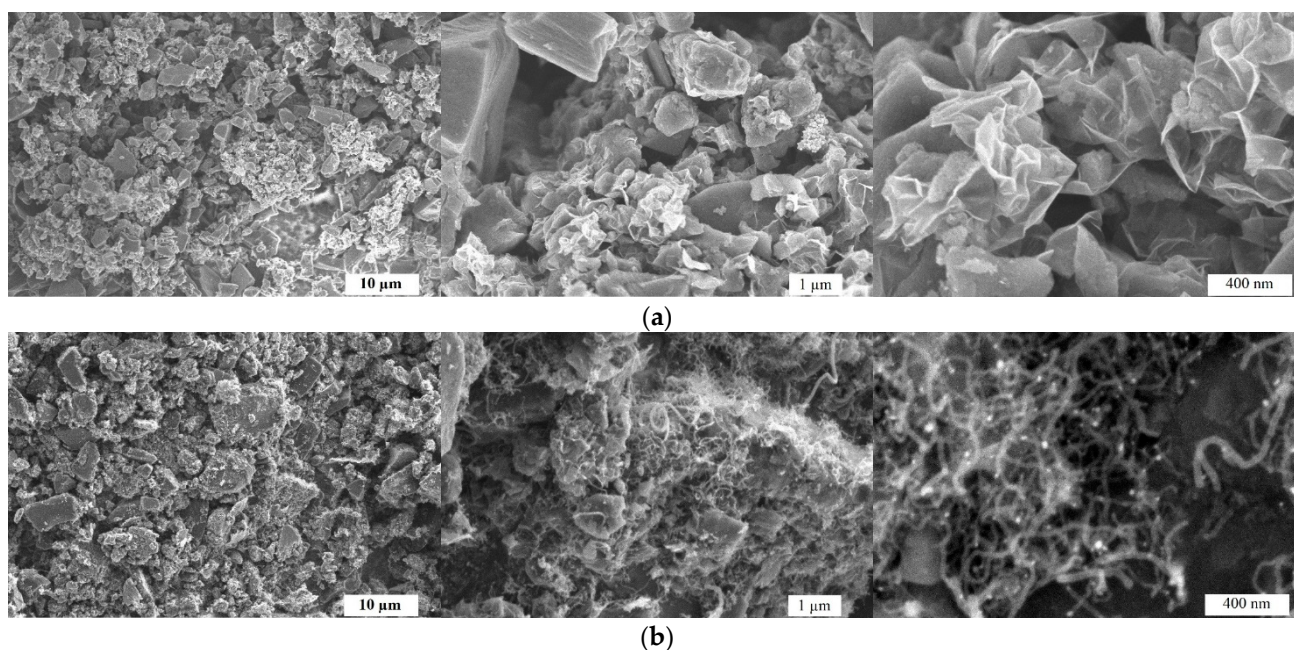


**Figure 1.** SEM images of AWC-N (a) and AWC-Ni-N (b) catalysts at different magnifications.

The characterization of the porous structure of the obtained doped carbon materials was carried out by determination of the surface area and pore-size distribution of the materials from nitrogen adsorption–desorption isotherms at 77 K (Figure 2). The isotherms



can be classified as type I according to the IUPAC and are characterized by type H4 hysteresis, which indicates the predominantly microporous structure with strong adsorbent–adsorptive interaction of these materials, with some contribution from mesoporosity [41]. It should be noted that nitrogen doping did not alter porosity of the activated carbons to any significant extent, which the authors of this paper have demonstrated previously [42].

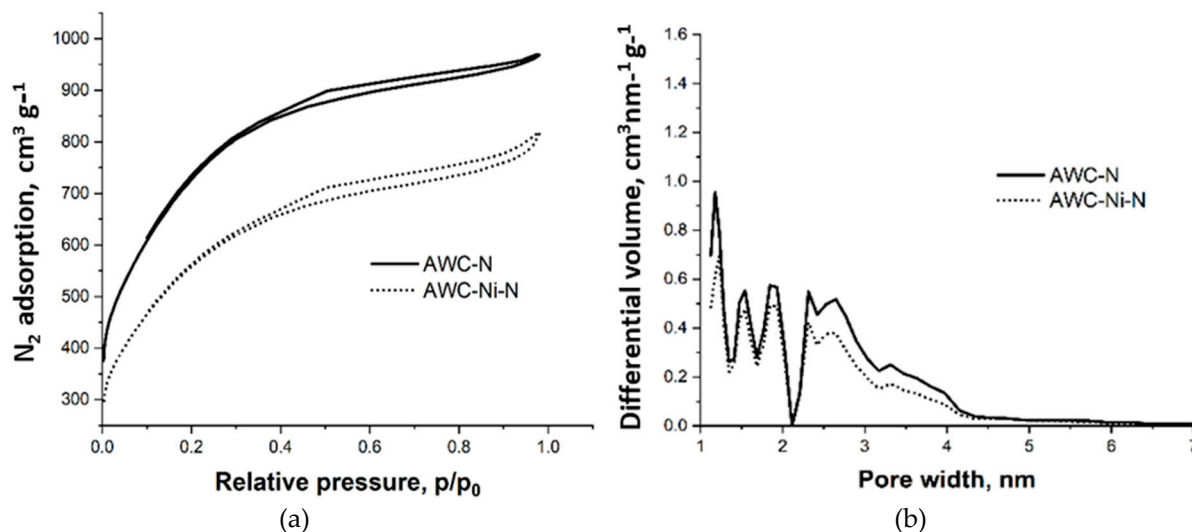


**Figure 2.** N<sub>2</sub> adsorption–desorption isotherms at 77 K (a) and pore-size distribution curves calculated from the corresponding isotherms by the density function theory (DFT) method (b) of nitrogen-doped activated carbon and nitrogen-doped activated-carbon-supported nickel particles.

The porous-structure parameters (Table 1) indicate differences in the textural properties of AWC-N and AWC-Ni-N catalysts. AWC-N had a slightly higher specific surface area (BET: 2217 m<sup>2</sup> g<sup>−1</sup>) compared with AWC-Ni-N (2050 m<sup>2</sup> g<sup>−1</sup>), as well as a larger pore volume (1.6 cm<sup>3</sup> g<sup>−1</sup> vs. 1.3 cm<sup>3</sup> g<sup>−1</sup>). A decrease in the specific surface area of AWC-Ni-N may have been related to an increase in the density of the material, as it was enriched with heavier Ni moieties, and to a possible partial blocking of the micropores by the Ni particles [7].

**Table 1.** Porous-structure parameters of the AWC-N and AWC-Ni-N catalysts.

Sample	Specific Surface Area, m <sup>2</sup> g <sup>−1</sup>			Pore Volume, cm <sup>3</sup> g <sup>−1</sup>			Average Pore Width, nm	Mesopores from V <sub>t</sub> , %
	BET	DR	DFT	Total	Micro	Meso		
AWC-N	2217	1921	1496	1.6	0.7	0.9	2.9	56.6
AWC-Ni-N	2050	1791	1387	1.3	0.6	0.6	2.5	49.7

The average pore width of AWC-N (2.9 nm) was marginally larger than that of AWC-Ni-N (2.5 nm). Additionally, the mesopore contribution to the total pore volume was higher in AWC-N (56.6%) compared with AWC-Ni-N (49.7%). This difference suggests that co-doping slightly reduced the porosity and the proportion of mesopores while potentially increasing the density of micropores or smaller pores. The main reason for this change was an increase in material density due to the introduction of metal/metal oxide particles into the structure as well as blockage of number of pores as the result of this process.

Figure 3 compares the 532 nm-excited Raman spectra of AWC-N and AWC-Ni-N catalysts. Both samples showed two strong bands visible at 1349–1360 cm<sup>−1</sup> and 1585–1586 cm<sup>−1</sup>, corresponding to prominent D and G modes of graphite, respectively. In addition, a well-defined feature at 2690–2694 cm<sup>−1</sup> was visible in the both samples. This feature belonged to the prominent 2D band and indicated an increase in the struc-

tural ordering of this carbon-based sample [43]. The important structural parameter in  $sp^2$ -hybridized layered carbon material was the average in-plane crystallite size  $L_a$  [44,45].

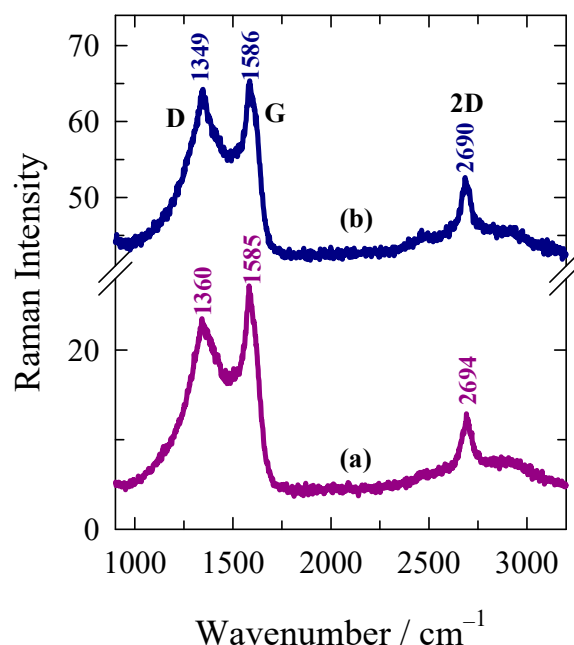


**Figure 3.** Raman spectra of carbon-based (a) AWC-N, and (b) AWC-Ni-N catalysts. Intensities were normalized to the intensity of G band. Spectra are shifted vertically for clarity. Excitation wavelength is 532 nm (0.4 mW).

The experimentally obtained  $\text{FWHM(G)}$  value can be used to determine the  $L_a$  [44,46,47]:

$$L_a = \frac{l_c}{2} \ln \left[ \frac{C}{\text{FWHM(G)} - \text{FWHM(G}_0\text{)}} \right] \quad (6)$$

where the photon coherence length  $l_c = 32$  nm,  $C = 95 \text{ cm}^{-1}$ , and  $\text{FWHM(G)}$  and  $\text{FWHM(G}_0\text{)}$  are the widths of the G band of sample under investigation and undoped pristine graphene ( $15 \text{ cm}^{-1}$ ), respectively. The equation is valid for measuring the  $L_a$  between 32 and 2.8 nm [44]. To estimate the  $\text{FWHM(G)}$  value, the experimental spectra in the frequency region from 1000 to  $1800 \text{ cm}^{-1}$  were fitted with five Gaussian- or Lorentzian-form components. The prominent D and G bands were fitted with Lorentzian-form functions and the additional  $D^*$  ( $1275 \text{ cm}^{-1}$ ) and  $D''$  ( $1520 \text{ cm}^{-1}$ ) bands with Gaussian-form functions. The presence of the  $D''$  band was associated with the amorphization of carbon material [2,47]. The relatively narrow disorder-induced  $D'$  band near  $1624 \text{ cm}^{-1}$  was also introduced into the fitting procedure. The  $\text{FWHM(G)}$  and estimated  $L_a$  values are given in Table 2.

**Table 2.** G-peak full width at half-maximum  $\text{FWHM(G)}$ , average crystallite size  $L_a$ , and intensity ratio  $I(D'')/I(G)$  of carbon-based samples.

Sample	$\text{FWHM(G)} (\text{cm}^{-1})$	$L_a (\text{nm})$	$I(D'')/I(G)$
AWC-N	55.7	13.6	0.51
AWC-Ni-N	49.8	16.1	0.55

In the case of AWC-N and AWC-Ni-N, the  $L_a$  varied from 13.6 to 16.1 nm, respectively. The larger in-plane crystallite size value was obtained for AWC-Ni-N. Another important structural parameter is the relative intensity of the  $D''$  band, measured as the intensity ratio  $I(D'')/I(G)$  [2]. This parameter probes the amorphization of the carbon material. The higher

ratio was found for the AWC-Ni-N catalyst indicating the higher amount of amorphous phase in this material.

XRD analysis was applied to determine the structure of the synthesized AWC-N and AWC-Ni-N catalysts (Figure 4). The diffraction peaks in both XRD patterns for AWC-N and AWC-Ni-N were located at around  $2\theta = 26.07^\circ$ ,  $43.37^\circ$ , and  $44.37^\circ$  and can be indexed to the (002), (100), and (101) planes of the graphite C (JCPDS card. No. 25–284). These peaks are characteristic of amorphous carbon or partially graphitized carbon, indicating that both materials retained an overall porous structure with significant disorder. The XRD pattern of AWC-Ni-N displayed peaks at  $2\theta \approx 37.23^\circ$ ,  $43.38^\circ$ ,  $44.22^\circ$ ,  $51.55^\circ$ ,  $63.04^\circ$ ,  $75.92^\circ$ , and  $79.77^\circ$  (Figure 4b). The diffraction peaks at  $44.22^\circ$ ,  $51.55^\circ$ , and  $75.92^\circ$  can be assigned to the (111), (200), and (220) planes of the face-centered cubic phase (fcc) of Ni (JCPDS card. no. 04–0850), while the peaks observed at  $37.23^\circ$ ,  $43.38^\circ$ ,  $63.04^\circ$ , and  $79.77^\circ$  can be indexed as the (111), (200), (220), and (222) lattice planes of the fcc NiO phase (JCPDS card. no. 47–1049). Incorporation of nickel into AWC-Ni-N resulted in the formation of new nickel-based crystalline phases and promoted the partial graphitization of the carbon material (Figure 4b).

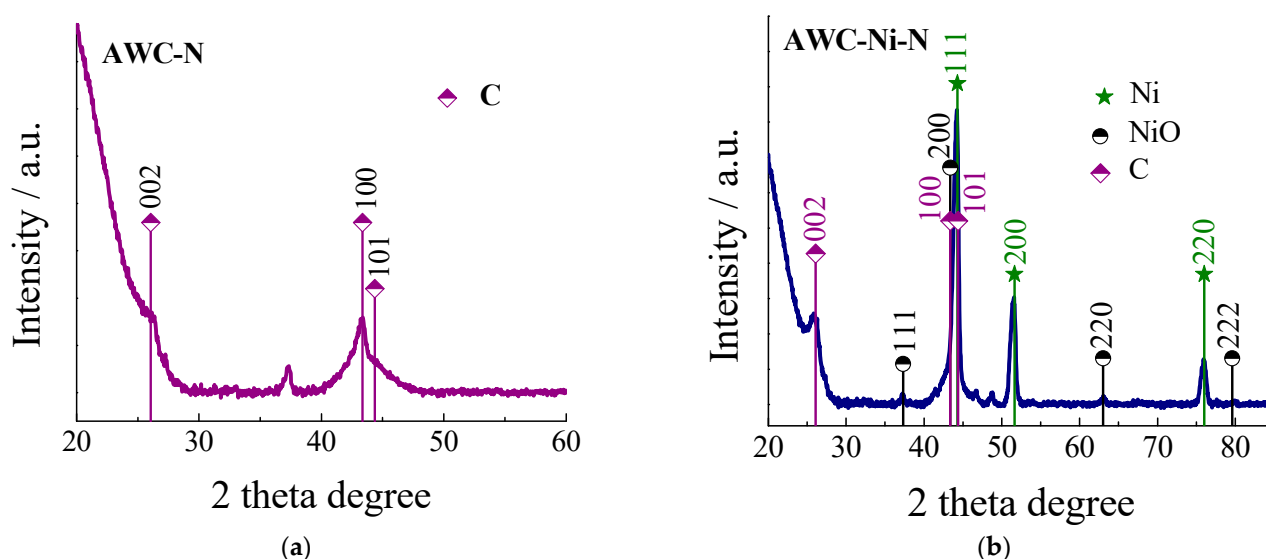


**Figure 4.** XRD patterns for the AWC-N (a) and AWC-Ni-N (b) catalysts.

These structural modifications may enhance the material's electrical conductivity and catalytic activity, making AWC-Ni-N more suitable for applications such as catalysis or energy storage.

XPS was used to analyze the elemental composition and bonding configurations of the AWC-N and AWC-Ni-N catalysts. Figure 5 shows the survey (a) and deconvoluted C 1s (b), N 1s (c), O 1s (d), and Ni 2p (e,f) high-resolution XPS spectra of the AWC-N and AWC-Ni-N catalysts. The presence and percentages of carbon, nitrogen, oxygen, and nickel species (Figure 5a) are shown in the survey XPS spectra. These are consistent with the XRD patterns. The high-resolution XPS C 1s spectra for the both catalysts were divided into four major peaks that appeared at 284.2 (Csp<sup>2</sup>), 284.7 (Csp<sup>3</sup>), 285.3 (N-sp<sup>2</sup>-C), and 286.2 ± 0.1 (N-sp<sup>3</sup>-C) (Figure 5b) [48]. Notably, most of carbon existed in the sp<sup>3</sup>-hybridized state (Table 3) [49,50]. The N 1s spectra were deconvoluted into two main pyridinic-N (~399 eV) and graphitic-N (~401 eV) peaks, respectively, for the AWC-N and AWC-Ni-N catalysts, respectively (Figure 5c). Most of the nitrogen was present in the catalytically active pyridinic-N form, which was higher (~65%) for the AWC-Ni-N catalyst prepared by a one-step doping of N and Ni compared with the AWC-N catalyst doped with N only (~48%) (Table 3).

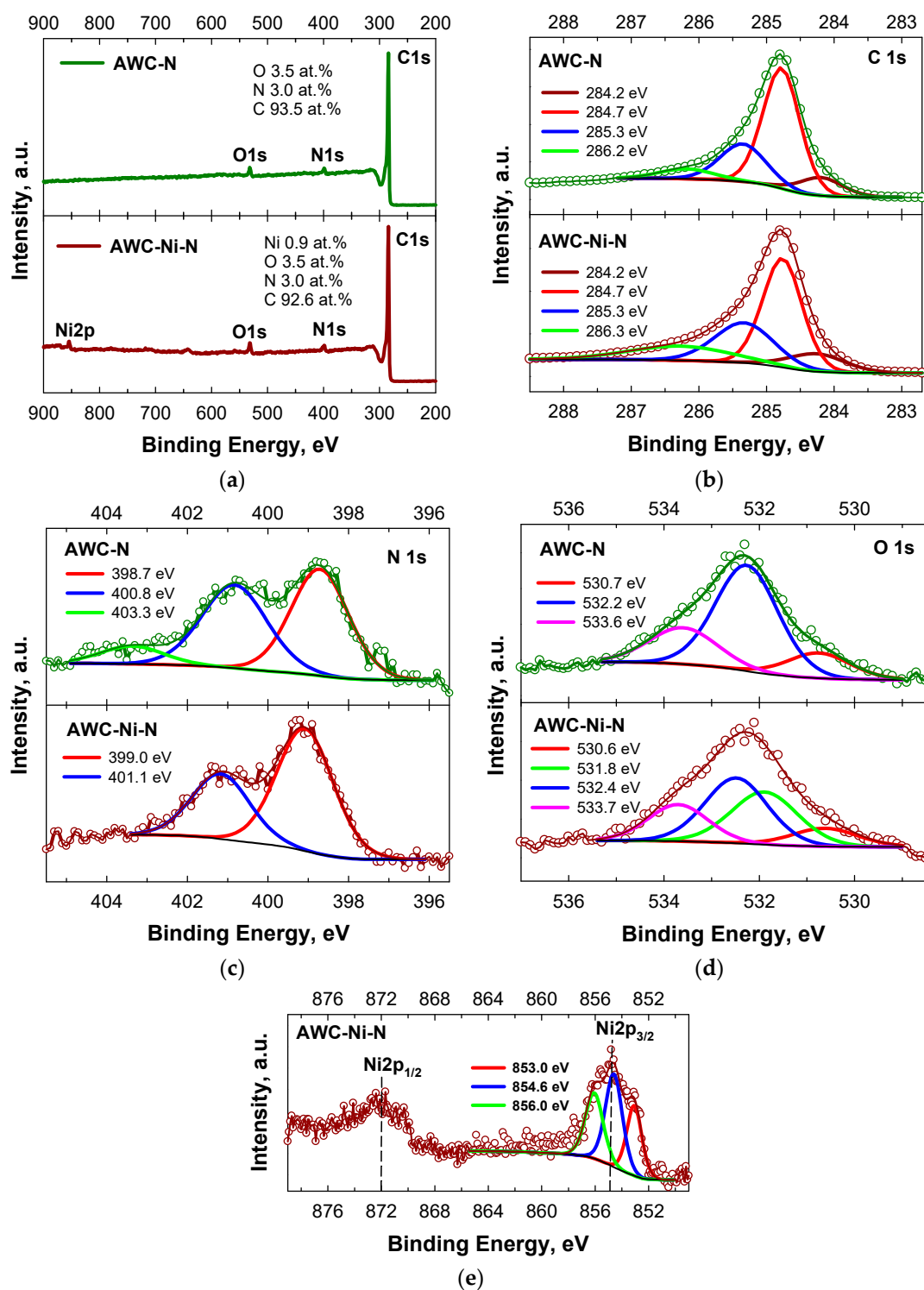


**Figure 5.** XPS of (a) survey, (b) C 1s, (c) N 1s, (d) O 1s, and (e) Ni 2p spectra of nitrogen-doped activated carbon (AWC-N) and nitrogen-doped activated-carbon-supported nickel nanoparticles (AWC-Ni-N).



**Table 3.** XPS analysis of the elemental composition of AWC-N and AWC-Ni-N.

Sample	C 1s		N 1s		O 1s		Ni 2p <sub>3/2</sub>	
	E <sub>b</sub> , eV	at. %	E <sub>b</sub> , eV	at. %	E <sub>b</sub> , eV	at. %	E <sub>b</sub> , eV	at. %
AWC-N	284.2	10.49	398.7	48.38	530.7	14.89		
	284.7	59.27	400.8	42.72	532.2	61.86		
	285.3	23.13	403.3	8.90	533.5	23.25		
	286.2	7.11						
AWC-Ni-N	284.2	11.02	399.0	64.79	530.6	10.91	853.0	27.71
	284.7	46.92	401.1	35.21	531.8	31.82	854.6	41.55
	285.3	26.00			532.4	37.26	856.0	30.75
	286.3	16.06			533.7	20.00		

The Ni 2p<sub>3/2</sub> spectrum could be deconvoluted to three component peaks, one at 853.0 eV, corresponding to Ni<sup>0</sup>, and the other two at 854.6 eV and 856.0 eV, corresponding, in the same way as NiO, to Ni<sup>2+</sup> (Figure 5e) [51–53]. The Ni metal 2p<sub>3/2</sub> peak position of 853.0 eV was within the literature value range of 852.7 eV ± 0.4 eV [54]. The binding energy of O 1s for the AWC-Ni-N catalyst was fitted as 530.6 eV (C–O–C, 10.91%), 531.8 eV (C–O–Ni, 31.82%), 532.1 eV (C=O/O–Ni, 37.26%), and 533.7 eV (C–OH/C–O–C, 20.0%), respectively (Table 3).

## 2.2. Determination of Electroactivity of Catalysts for the HzOR

The electrocatalytic activity of the AWC-N and AWC-Ni-N catalysts was evaluated toward the HzOR in alkaline media. The activity of the prepared AWC-N and AWC-Ni-N catalysts was evaluated by cyclic voltammetry by recording CVs in 1 M KOH solution containing different concentrations of N<sub>2</sub>H<sub>4</sub> in the potential range of −1.2 V to 0.2 V (vs. SCE) at an electrode-potential scan rate of 50 mV s<sup>−1</sup> (Figure 6a,b). Figure 6c shows the stabilized (5th) LSVs for both catalysts in the same solution.

In 1 M KOH solutions (Figure 6a,b, black lines), the current density remained relatively low, indicating limited electrochemical activity when using the AWC-N and AWC-Ni-N catalysts. The current density increased significantly when 0.05 M N<sub>2</sub>H<sub>4</sub> was added, especially in the positive potential region, indicating that the HzOR (Equation (6)) occurred on both AWC-N (Figure 6a, blue line) and AWC-Ni-N (Figure 6b, dark pink line) catalysts. Both catalysts demonstrated characteristic oxidation peaks in the presence of N<sub>2</sub>H<sub>4</sub>, with AWC-Ni-N exhibiting sharper and higher peaks. This suggests that the incorporation of nickel enhanced the kinetics of the oxidation reaction. The onset potential for the HzOR occurred at potentials of −0.52 and −0.56 V for AWC-Ni-N and AWC-N, respectively. The peak HzOR values on the AWC-Ni-N catalyst were obtained at more negative potentials of −0.26 V (Figure 6c, dark pink line) as compared with that for AWC-N (−0.07 V) (Figure 6c, blue line), indicating it's a superior electrocatalytic activity for hydrazine oxidation. The enhanced electrocatalytic activity of the AWC-Ni-N catalyst for hydrazine oxidation can be attributed to the formation of nickel-based active sites, such as metallic Ni or NiO, which improved hydrazine adsorption and activation. In addition, the AWC-Ni-N catalyst, which was doped with both nitrogen and nickel, exhibited a more compact structure with interconnected particles and distinctive wire-like nanostructures. These wire-like nanostructures, likely formed due to the catalytic influence of nickel during the co-doping process, were absent in the AWC-N catalyst. These web-like carbon fibers might have contributed to an increased surface area and enhanced conductivity. In contrast, the AWC-N catalyst, doped with nitrogen only, displayed a highly porous, rough, and irregular morphology. The inclusion of nickel significantly enhanced the efficiency of the oxidation process.

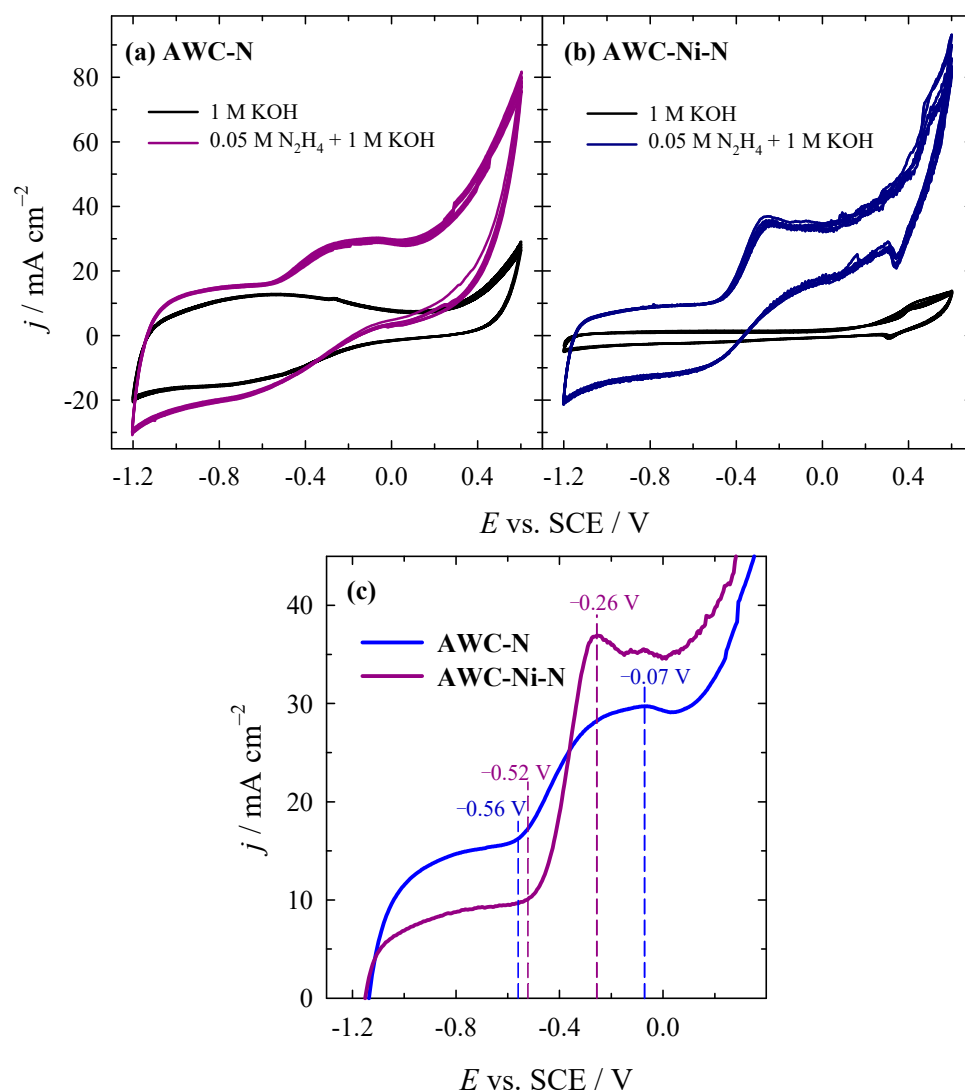


**Figure 6.** CVs of AWC-N (a) and AWC-Ni-N (b) catalysts recorded in 1 M KOH and 0.05 M  $\text{N}_2\text{H}_4$  + 1 M KOH at  $50 \text{ mV s}^{-1}$ ,  $T = 25^\circ\text{C}$ . (c) LSVs of stabilized (5th) cycles for AWC-N and AWC-Ni-N in the same solution.

In addition, the dependence of the HzOR on the  $\text{N}_2\text{H}_4$  concentration and on the scan rate was determined for both catalysts. Figure 7 shows the LSVs recorded on both catalysts in 1 M KOH solution containing different amounts of  $\text{N}_2\text{H}_4$ . As the concentration of  $\text{N}_2\text{H}_4$  increased in the 1 M KOH solution (0.025–0.10 M), the measured current density also increased. This increase was observed in both the AWC-N and AWC-Ni-N catalysts (see Figure 7a,b).

In addition, the current density values increased by approximately two and three times as the  $\text{N}_2\text{H}_4$  concentration increased from 25 to 100 mM recorded on the AWC-N and AWC-Ni-N catalysts, respectively. The insets in both graphs show a linear relationship between the peak current density and  $\text{N}_2\text{H}_4$  concentration, indicating that the reaction kinetics were concentration-dependent, likely governed by a diffusion-controlled mechanism. AWC-Ni-N exhibited significantly higher current densities than AWC-N under identical conditions, highlighting the enhanced catalytic performance of the nickel-doped material.

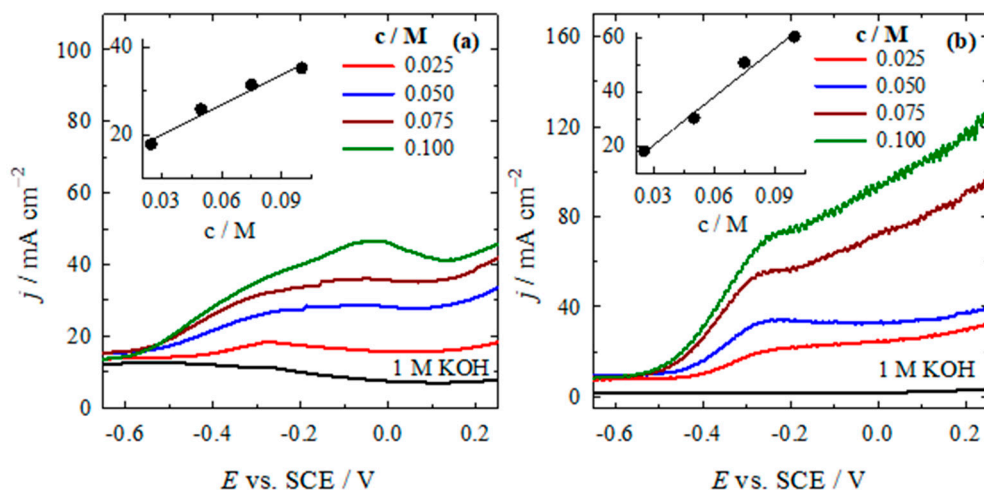


**Figure 7.** LSVs of AWC-N (a) and AWC-Ni-N (b) catalysts recorded in 0.025–0.10 M  $\text{N}_2\text{H}_4$  + 1 M KOH at  $50 \text{ mV s}^{-1}$ ,  $T = 25^\circ\text{C}$ .

The dependence of the HzOR current densities for the AWC-N and AWC-Ni-N catalysts, recorded in a solution of 0.05 M  $\text{N}_2\text{H}_4$  and 1 M KOH, on different potential scan rates is shown in Figure 8. The AWC-Ni-N catalyst (Figure 8b) exhibited a higher current density compared with the AWC-N catalyst (Figure 8a) under similar conditions, indicating that the incorporation of Ni enhanced the catalytic activity. For both catalysts, as the scan rate increases from 10 to  $50 \text{ mV s}^{-1}$ , the peak current density increased by approximately three times for the AWC-N catalyst and two times for the AWC-Ni-N catalyst. The insets in both graphs show a linear relationship between the peak current density and the scan rate, with  $R^2 > 0.99$ . This strong correlation suggests that the electrochemical reactions at the electrode for both catalysts were diffusion-controlled. Overall, the AWC-Ni-N catalyst demonstrated superior catalytic performance compared with AWC-N, making it more suitable for applications involving the HzOR.

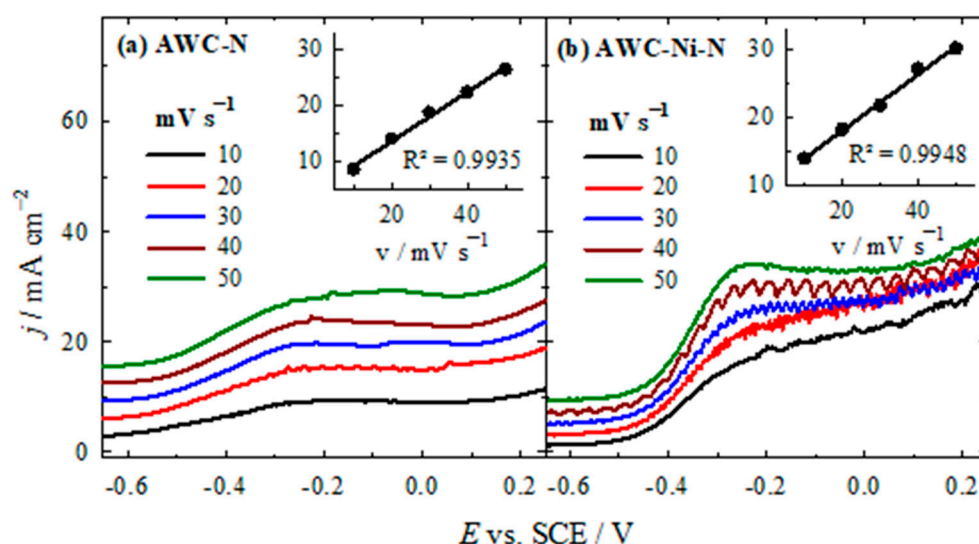


**Figure 8.** LSVs of AWC-N (a) and AWC-Ni-N (b) catalysts recorded in 0.05 M  $\text{N}_2\text{H}_4$  + 1 M KOH at different potential scan rates,  $T = 25^\circ\text{C}$ .

Figure 9 illustrates the chronoamperometric (CA) curves representing the catalytic activities of two different catalysts, AWC-N (black line) and AWC-Ni-N (blue line), tested for the electro-oxidation reaction of  $\text{N}_2\text{H}_4$  in an electrolyte solution containing 0.05 M  $\text{N}_2\text{H}_4$

and 1 M KOH at a constant applied potential of  $-0.3$  V (vs. SCE) and maintained at room temperature ( $25$  °C).

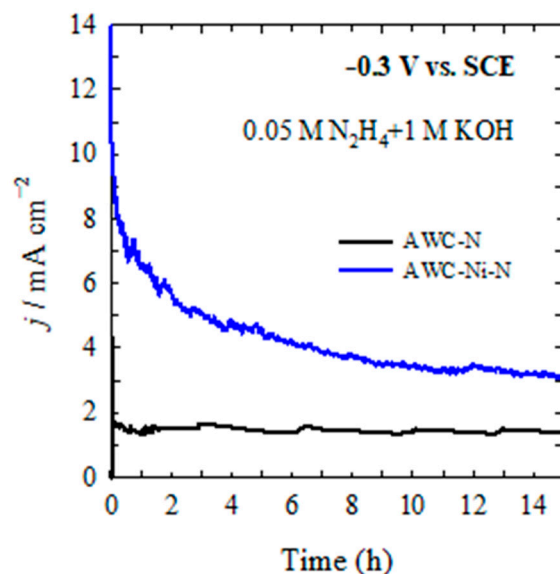


**Figure 9.** CA of AWC-N (black line) and AWC-Ni-N (blue line) catalysts recorded in  $0.05$  M  $\text{N}_2\text{H}_4$  +  $1$  M KOH at  $-0.3$  V vs. SCE,  $T = 25$  °C.

During the initial stage ( $0$ – $1.4$  h), a significantly higher current density was observed, approximately  $10$   $\text{mA cm}^{-2}$  at time zero, indicating rapid catalytic activity and excellent initial catalytic efficiency. However, there was a noticeable rapid decrease in current density during this initial period, likely due to the rapid stabilization of catalytic sites, consumption or rearrangement of active species, or partial deactivation of catalyst. The AWC-N catalyst showed a much lower current density, approximately  $1.5$  to  $2$   $\text{mA cm}^{-2}$ , compared with the AWC-Ni-N catalyst, and displayed a stable, nearly constant current density throughout this initial interval, suggesting moderate initial activity but good immediate stability. During the intermediate stage ( $1.4$ – $8.3$  h), the current density for the AWC-Ni-N catalyst continued to gradually decrease, showing a slow but steady decline from approximately  $5$ – $6$   $\text{mA cm}^{-2}$  at around  $1.4$  h to nearly  $4$   $\text{mA cm}^{-2}$  at  $8.3$  h. This gradual decay may have reflected slow surface changes, the loss of some active sites, or the formation of surface species that partially blocked or modified the catalyst sites. The current density of AWC-N remained consistently stable around  $1$ – $2$   $\text{mA cm}^{-2}$  over the same time period, maintaining its lower but stable catalytic activity without noticeable degradation. At the long-term or steady-state stage ( $8.3$ – $13.9$  h), the AWC-Ni-N catalyst reached a nearly stable steady-state current density of  $3$ – $4$   $\text{mA cm}^{-2}$ , indicating sustained catalytic activity even after prolonged exposure to reaction conditions. This final stabilized current density was significantly higher (approximately double) compared with the AWC-N catalyst, highlighting the enhanced long-term catalytic performance and stability. The AWC-N catalyst remained largely stable, maintaining a steady-state current density of around  $1$ – $2$   $\text{mA cm}^{-2}$ , indicating that, although its catalytic activity was comparatively lower, it exhibited high operational stability under long-term test conditions.

The CA curves clearly show that incorporating Ni into the AWC-N structure, forming the AWC-Ni-N catalyst, significantly improved catalytic performance in  $\text{N}_2\text{H}_4$  oxidation. Although there was an initial drop from a high initial current density, the AWC-Ni-N catalyst maintained superior activity and good long-term stability compared with the unmodified AWC-N catalyst. In contrast, the AWC-N catalyst, although highly stable, showed relatively low catalytic activity throughout the test period. Overall, the data in

Figure 9 strongly support the conclusion that the AWC-Ni-N catalyst offered significantly improved catalytic efficiency and durability for  $\text{N}_2\text{H}_4$  electro-oxidation compared with the AWC-N catalyst alone.

### 2.3. Performance of Direct $\text{N}_2\text{H}_4\text{-H}_2\text{O}_2$ Fuel Cell

For potential application in a direct  $\text{N}_2\text{H}_4\text{-H}_2\text{O}_2$  fuel cell, the performance and stability of the AWC-N and AWC-Ni-N catalysts were evaluated. A direct  $\text{N}_2\text{H}_4\text{-H}_2\text{O}_2$  single fuel cell was constructed using the AWC-N and AWC-Ni-N catalysts as both anodes and cathodes. The performance of the  $\text{N}_2\text{H}_4\text{-H}_2\text{O}_2$  system is strongly influenced by the choice of electrode materials, the membrane separator, and the electrolyte composition. Based on previous studies of different catholyte and anolyte compositions, a catholyte consisting of 5 M  $\text{H}_2\text{O}_2$  + 1.5 M HCl and an anolyte of 1 M  $\text{N}_2\text{H}_4$  + 1 M KOH were used in the present study. The separator used was a standard Nafion<sup>®</sup> N117 membrane. Figure 10 presents the fuel-cell polarization and corresponding power density curves for the AWC-N and AWC-Ni-N catalysts at temperatures of 25, 35, 45, and 55 °C.

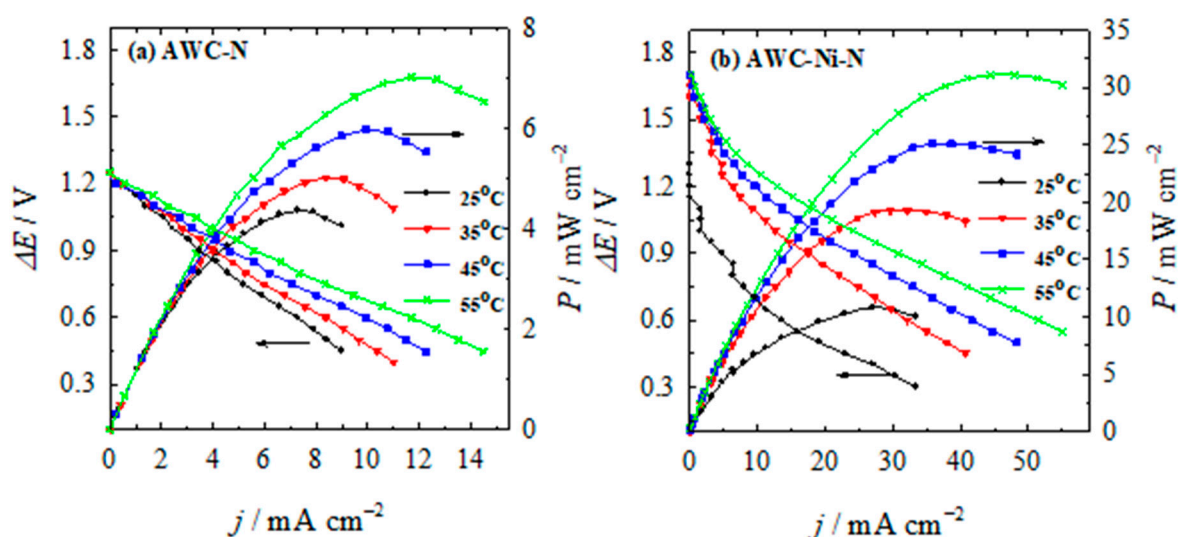


**Figure 10.** Cell polarization and power density curves for the direct  $\text{N}_2\text{H}_4\text{-H}_2\text{O}_2$  fuel cell using (a) AWC-N and (b) AWC-Ni-N catalysts as the anodes/cathodes with anolyte consisting of 1 M  $\text{N}_2\text{H}_4$  and 1 M KOH and 5 M  $\text{H}_2\text{O}_2$  and 1.5 M HCl catholyte at different temperatures.

Polarization curves were run in triplicate, and no significant loss of activity was observed. The overlapping curves between repetitions show that the AWC-N and AWC-Ni-N electrocatalysts had excellent stability. The key fuel-cell performance parameters determined from these tests are summarized in Table 4. The fuel cell displayed an open circuit voltage of approximately 1.25 V and 1.7 V using AWC-N and AWC-Ni-N as the anode and cathode catalysts, respectively. It was observed that the power density achieved with the AWC-Ni-N catalyst was significantly higher than that obtained with the AWC-N catalyst (Figure 10, Table 4). Peak power densities of up to  $10.8 \text{ mW cm}^{-2}$  were achieved at 25 °C, corresponding to a current density of  $27 \text{ mA cm}^{-2}$  and a cell voltage of 0.4 V (Figure 10), when the AWC-Ni-N catalyst was used as both anode and cathode. In addition, the peak power-density values increased by approximately 1.6 times and 2.9 times for the AWC-N and AWC-Ni-N catalysts, respectively, when the operating temperature was increased from 25 °C to 55 °C.



**Table 4.** Electrochemical parameters of the  $\text{N}_2\text{H}_4\text{-H}_2\text{O}_2$  employing the AWC-N and AWC-Ni-N anode/cathode catalysts.

Catalyst	T (°C)	Peak Power Density ( $\text{mW cm}^{-2}$ )	<i>j</i> at Peak Power Density ( $\text{mA cm}^{-2}$ )	<i>E</i> at Peak Power Density (V)
AWC-N	25	4.4	7.3	0.60
	35	5.0	8.4	0.60
	45	6.0	9.9	0.60
	55	7.0	11.7	0.60
AWC-Ni-N	25	10.8	27.0	0.40
	35	19.3	32.2	0.60
	45	25.1	38.6	0.65
	55	31.1	47.9	0.65

The performance difference between AWC-N and AWC-Ni-N can be attributed to the enhanced electrocatalytic activity of Ni-incorporated catalysts. The presence of Ni-based active sites (such as metallic Ni and NiO) likely promoted more efficient hydrazine oxidation at the anode, reducing activation losses and improving overall fuel-cell efficiency. Additionally, the nitrogen-doped carbon network in AWC-Ni-N enhanced electrical conductivity, facilitating faster electron transfer. Furthermore, the wire-like nanostructure of AWC-Ni-N improved mass transport, ensuring better fuel utilization and higher reaction rates. The significant increase in peak power density at elevated temperatures suggests that higher operating temperatures enhanced reaction kinetics and mass diffusion, contributing to improved cell performance. These factors collectively explain why AWC-Ni-N achieved superior performance compared with AWC-N in the direct  $\text{N}_2\text{H}_4\text{-H}_2\text{O}_2$  fuel cell.

Table 5 compares various catalyst systems and their performance in direct hydrazine-based fuel cells, with a specific emphasis on their maximum power densities ( $P_{\text{max}}$ ), operating temperatures, and electrolyte conditions. The developed catalyst (AWC-Ni-N) showed a significant enhancement in room-temperature catalytic performance compared with the unmodified AWC-N, and was competitive with other room-temperature catalysts, such as Ni–Co–Se nanorods and metal-foam catalysts. Although it did not outperform high-temperature Pd–Ni- or Pt–Cu-based catalysts, it represents a valuable balance between cost, complexity, and efficiency, making it a promising option for practical and economically viable low-temperature  $\text{N}_2\text{H}_4$  fuel-cell applications.

**Table 5.** The comparison of  $\text{N}_2\text{H}_4\text{-H}_2\text{O}_2$  performance using different electrocatalysts and anolyte–catholyte compositions.

Anode	Cathode	Anolyte	Catholyte	$P_{\text{max}}$ , $\text{mW cm}^{-2}$	T, (°C)	Ref.
AWC-N	AWC-N	1 M $\text{N}_2\text{H}_4$ + 1 M KOH	5 M $\text{H}_2\text{O}_2$ + 1.5 M HCl	4.4 7.0	25 55	[This work]
AWC-Ni-N	AWC-Ni-N	1 M $\text{N}_2\text{H}_4$ + 1 M KOH	5 M $\text{H}_2\text{O}_2$ + 1.5 M HCl	10.8 31.1	25 55	[This work]
$\text{Ni}_{0.5}\text{Co}_{0.5}\text{Se}_2$	$\text{Ni}_{0.5}\text{Co}_{0.5}\text{Se}_2$	4.0 M KOH	0.5 $\text{H}_2\text{SO}_4$	13.3	25	[55]
Pd–Ni/NrGO (1.0 $\text{mg cm}^{-2}$ )	Pt/C (0.5 $\text{mg cm}^{-2}$ )	1.0 M $\text{N}_2\text{H}_4$ + 2.0 M NaOH	2 M $\text{H}_2\text{O}_2$ + 0.5 M $\text{H}_2\text{SO}_4$	187.9 216.7	25 60	[56]
$\text{Pt}_{53}\text{Cu}_{47}/\text{C}$ (0.5 $\text{mg cm}^{-2}$ )	Pt/C (20 wt.%) (1.0 $\text{mg cm}^{-2}$ )	1.0 M $\text{N}_2\text{H}_4$ + 1.0 M KOH	$\text{O}_2$ flow rate: 30 SCCM	56.1	80	[57]
$\text{Ni}_{0.6}\text{Co}_{0.4}$ nanosheets (1.4 $\text{mg cm}^{-2}$ )	Pt/C (40.0 wt.%)	20wt% M $\text{N}_2\text{H}_4$ + 4.0 M KOH	20.0% $\text{H}_2\text{O}_2$ + 0.5 M $\text{H}_2\text{SO}_4$	107.1	80	[58]
Ni foam@Ag–Ni	Pd/CFC	0.045 M $\text{N}_2\text{H}_4$ + 1 M KOH	1 M $\text{H}_2\text{O}_2$ + 2 M $\text{H}_2\text{SO}_4$	6.7	-	[59]
Ni foam@Ni	Pd/CFC	0.045 M $\text{N}_2\text{H}_4$ + 1 M KOH	1 M $\text{H}_2\text{O}_2$ + 2 M $\text{H}_2\text{SO}_4$	4.1	-	[59]

### 3. Materials and Methods

#### 3.1. Preparation of Nitrogen-Doped Activated-Carbon-Supported Nickel Particles

Alder wood char (Ltd. "Fille", Valmiera, Latvia) was used as a carbon precursor. Activated carbon material (AWC) was synthesized by mixing 50 g of char with 150 g of NaOH, following an activation procedure at a temperature of 800 °C for 2 h in an argon (Ar) atmosphere using a muffle furnace. After cooling, the AWC material was demineralized by treatment with a 10% hydrochloric acid (HCl) solution for 2 h. The material was washed with demineralized water until the pH stabilized at 5–6, and then dried in an oven at  $105 \pm 2$  °C for 12 h.

Doping of the obtained activated carbon (AWC) with nickel and nitrogen was performed in a single step and the resulting material was designated as AWC-Ni-N. The mixture of 2 g AWC, 40 g dicyandiamide (DCDA), and 0.62 g nickel acetate ( $\text{Ni}(\text{CH}_3\text{COO})_2$ ) was soaked in 250 mL dimethylformamide (DMF) for two hours, followed by evaporation of DMF in rotary evaporator and treatment of the resulting solid residue at a temperature of 800 °C for 1 h under an Ar atmosphere in muffle oven. Nitrogen-doped activated carbon (AWC-N) was synthesized for the comparison using the similar approach. AWC was doped with nitrogen by dispersing it in a solution of DCDA and DMF, with the same mass ratio of carbon to DCDA of 1:20. After solvent removal with a rotary evaporator, the resulting mixture was treated at 800 °C for 1 h in an Ar atmosphere in muffle oven.

#### 3.2. Characterization of Catalysts

The structural and surface morphology of the synthesized materials was examined using a Helios NanoLab 650 SEM/FIB workstation, equipped with an INCA Energy 350 X-Max 20 energy dispersive X-ray (EDX) spectrometer (Oxford Instruments, Abingdon, UK).

The textural properties, including porous structure, specific surface area, total volumes of micro- and mesopores, and pore-size distribution, were determined from isotherms of low-temperature adsorption–desorption of nitrogen at 77 K. Isotherms were recorded using a Nova 4200e device (Quantachrome, Boynton Beach, FL, USA). Samples were degassed for 3 h at 300 °C before each test.

An inVia Raman spectrometer (Renishaw, New Mills, UK), equipped with a thermoelectrically cooled ( $-70$  °C) CCD camera and microscope, was used for Raman spectra recording. The Raman signal was excited with 532 nm radiation from a pumped solid state (DPSS) laser (Renishaw, UK). The Raman spectra were recorded using the  $20\times/0.40$  NA objective lens and 1800 lines/mm grating. The accumulation time was 40 s. The laser power at the sample was limited to 0.4 mW to avoid sample degradation. Calibration of the Raman frequencies was done using the polystyrene standard. The parameters of the bands were determined by fitting the experimental spectra with Gaussian- and Lorentzian-shaped components using GRAMS/A1 8.0 software (Thermo Scientific, East Grinstead, UK).

The chemical composition of the samples was analyzed using the Kratos AXIS Supra+ spectrometer (Kratos Analytical, UK, Manchester, 2019) with monochromatic Al K $\alpha$  (1486.6 eV) X-ray radiation powered at 225 W. Binding energies were referenced to the adventitious C 1s peak at 284.8 eV. The XPS data were converted to the VAMAS format and processed using the Advantage software 5.9931.0.6755 (Thermo Scientific, East Grinstead, UK). The base pressure in the analysis chamber was less than  $1 \times 10^{-8}$  mbar, and a low electron flood gun was used as a charge neutralizer. Survey scans were recorded at a pass energy of 80 eV with an energy step of 1 eV, while high-resolution spectra (pass energy—10 eV, in 0.1 eV steps) were recorded over individual element peaks.

X-ray diffraction (XRD) analysis was performed using a D2 PHASER diffractometer (Bruker, Karlsruhe, Germany), employed with Cu-K-alpha as the X-ray source. Measurements were conducted in the  $2\theta$  range from  $10^\circ$  to  $90^\circ$  in step-scan mode with the step size of  $0.02^\circ$  and counting time of 1 s per step.

### 3.3. Electrochemical Measurements

Electrochemical characterization was carried out in a conventional three-electrode setup of 100 mL connected to a PGSTAT302 potentiostat (Metrohm Autolab B.V., Utrecht, The Netherlands), controlled via the Nova 2.1.4 software. The working electrodes utilized in this study were the AWC-N and AWC-Ni-N catalysts, which were coated on the glassy carbon (GC) electrode with a geometric area of  $0.2\text{ cm}^2$ . The ink was prepared by dispersing 21.5 mg of the catalysts in 1 mL of a  $\text{C}_2\text{H}_5\text{OH}:\text{H}_2\text{O}$  (vol 1:1) solution and mixed with 8  $\mu\text{L}$  of a 5 wt.% Nafion solution. Then, 8  $\mu\text{L}$  of the obtained ink was deposited on a pretreated GC electrode surface, resulting in a catalyst loading of  $0.8764\text{ mg}_{\text{cat}}\text{ cm}^{-2}$ .

A Pt sheet served as the counter electrode, and a saturated calomel electrode (SCE) was used as the reference electrode. The HzOR studies were performed by recording cyclic voltammograms (CVs) in an Ar-deaerated solution of 0.05 M  $\text{N}_2\text{H}_4$  and 1 M KOH, as well as in the background solution of 1 M KOH at room temperature. The potential was cycled in the range of  $-1.2$  to  $0.6\text{ V}$  (versus SCE) at various scan rates from 10 to  $50\text{ mV s}^{-1}$ . Additional CV measurements were conducted with different concentrations of  $\text{N}_2\text{H}_4$  in the range from 25 to 100 mM at a fixed scan rate of  $50\text{ mV s}^{-1}$ .

### 3.4. Fuel-Cell Test Experiments

Direct  $\text{N}_2\text{H}_4\text{-H}_2\text{O}_2$  fuel-cell experiments were done by employing the AWC-N and AWC-Ni-N catalysts with a geometric area of  $1\text{ cm}^2$  as the anode and as the cathode. An alkaline solution containing 1 M  $\text{N}_2\text{H}_4$  and 1 M KOH was used as the anolyte, whereas the catholyte contained 5 M  $\text{H}_2\text{O}_2$  and 1.5 M HCl. Each compartment of the cell was filled with 100 mL of the freshly prepared electrolytes. A Nafion N117 membrane was used for separation of the anodic and cathodic compartments of the single direct  $\text{N}_2\text{H}_4\text{-H}_2\text{O}_2$  fuel cell. The current densities shown were normalized to the geometric area of the catalysts. Electrochemical measurements were assessed using a Zennium workstation (ZAHNER-Elektrik GmbH & Co., KG, Kronach, Germany). Cell polarization curves were recorded at temperatures between 25 and  $55^\circ\text{C}$ .

## 4. Conclusions

In this study, efficient biomass-derived carbon catalysts were synthesized. It was found that nitrogen and nickel doping profoundly affected the properties of biomass-derived carbon catalysts. Nitrogen doping introduced a porous structure and a high surface area, while nickel co-doping further modified the morphology, enhanced the structural ordering, and significantly improved the electrocatalytic activity for both hydrazine oxidation. The AWC-Ni-N catalyst, which was doped with both nitrogen and nickel, demonstrated higher electrocatalytic activity for hydrazine oxidation compared with the AWC-N catalyst, doped with nitrogen only. The oxidation of  $\text{N}_2\text{H}_4$  over these catalysts was controlled by the diffusion of reactants to the catalyst surface. Overall, the AWC-N and AWC-Ni-N catalysts show promise as anode/cathode materials for  $\text{N}_2\text{H}_4\text{-H}_2\text{O}_2$  fuel cells. The fuel cells exhibited voltages of approximately 1.25 V and 1.7 V, employing AWC-N and AWC-Ni-N as the anode and cathode catalysts, respectively. The fuel cell incorporating AWC-Ni-N as both the anode and cathode achieved a significantly higher power density than the fuel cell using AWC-N. This improved performance is attributed to the superior catalytic activity of AWC-Ni-N for hydrazine oxidation. Nickel- and nitrogen-co-doped carbon catalysts

are promising materials for energy conversion applications. The use of nickel as the active metal avoids the need for more expensive noble metals, such as platinum, palladium, and ruthenium, without compromising catalytic efficiency.

**Author Contributions:** Conceptualization, L.T.-T., A.B. and E.N.; methodology, V.U.; validation, A.Z., L.T.-T. and E.N.; formal analysis, A.V. and G.D.; investigation, V.U., A.P., A.V., G.N. and D.U.; data curation, A.V.; writing—original draft preparation, A.B., D.U. and A.P.; writing—review and editing, L.T.-T., A.P. and G.N.; visualization, V.U., A.P., A.B. and G.N.; supervision, G.D., A.Z. and E.N. All authors have read and agreed to the published version of the manuscript.

**Funding:** This research was supported by grants from Iceland, Liechtenstein, and Norway through the EEA Grants according to the project contract with the Research Council of Lithuania (LMTLT) No. S-BMT-21-12 (LT08-2-LMT-K-01-055).

**Data Availability Statement:** The original contributions presented in this study are included in the article. Further inquiries can be directed to the corresponding author(s).

**Acknowledgments:** The authors would like to thank Vitalija Jasulaitienė for characterizing the samples by X-ray photoelectron spectroscopy (XPS).

**Conflicts of Interest:** The authors declare no conflicts of interest.

## References

1. Kong, Z.; Zhang, H.; Zhou, T.; Xie, L.; Wang, B.; Jiang, X. Biomass-derived functional materials: Preparation, functionalization, and applications in adsorption and catalytic separation of carbon dioxide and other atmospheric pollutants. *Sep. Purif. Technol.* **2025**, *354*, 129099. [\[CrossRef\]](#)
2. Upskuvienė, D.; Balčiūnaitė, A.; Drabavičius, A.; Jasulaitienė, V.; Niaura, G.; Talaikis, M.; Plavniece, A.; Dobeles, G.; Volperts, A.; Zhurinskis, A.; et al. Synthesis of nitrogen-doped carbon catalyst from hydrothermally carbonized wood chips for oxygen reduction. *Catal. Commun.* **2023**, *184*, 106797. [\[CrossRef\]](#)
3. Zhang, X.; Li, S.; Zhao, G.; Zhao, H.; Zhou, M. Single-atom catalysts toward electrochemical water treatment. *Appl. Catal. B Environ. Energy* **2025**, *363*, 124783. [\[CrossRef\]](#)
4. Zhu, Z.; Men, Y.; Zhang, W.; Yang, W.; Wang, F.; Zhang, Y.; Zeng, X.; Xiao, J.; Tang, C.; et al. Versatile carbon-based materials from biomass for advanced electrochemical energy storage systems. *Escience* **2024**, *4*, 100249. [\[CrossRef\]](#)
5. Fu, Q.; Li, N.; Lu, K.; Dong, Z.; Yang, Y. The emerging development of nitrogen and sulfur co-doped carbon dots: Synthesis methods, influencing factors and applications. *Mater. Today Chem.* **2024**, *37*, 102032. [\[CrossRef\]](#)
6. Palm, I.; Kibena-Pöldsepp, E.; Mooste, M.; Kozlova, J.; Käärik, M.; Kikas, A.; Treshchalov, A.; Leis, J.; Kisand, V.; Tamm, A.; et al. Nitrogen and sulphur co-doped carbon-based composites as electrocatalysts for the anion-exchange membrane fuel cell cathode. *Int. J. Hydrogen Energy* **2024**, *55*, 805–814. [\[CrossRef\]](#)
7. Volperts, A.; Upskuvienė, D.; Balčiūnaitė, A.; Jasulaitienė, V.; Niaura, G.; Drabavičius, A.; Plavniece, A.; Dobeles, G.; Zhurinskis, A.; Lin, Y.-C.; et al. Copper-nitrogen dual-doped activated carbon derived from alder wood as an electrocatalyst for oxygen reduction. *Catal. Commun.* **2023**, *182*, 106743. [\[CrossRef\]](#)
8. Pereira, G.M.; Cellet, T.S.P.; Winkler, M.E.G.; Rubira, A.F.; Silva, R. Printing specific active sites for ORR and hydrazine oxidation on N-doped carbon. *Mater. Chem. Phys.* **2023**, *307*, 128102. [\[CrossRef\]](#)
9. Song, S.; Li, Y.; Shi, Y.; Xu, Y.; Niu, Y. Oxygen-doped MoS<sub>2</sub> nanoflowers with sulfur vacancies as electrocatalyst for efficient hydrazine oxidation. *J. Electroanal. Chem.* **2022**, *906*, 115986. [\[CrossRef\]](#)
10. Taghaddosi, S.; Rezaee, S.; Shahrokhian, S. Facile synthesis of N-doped hollow carbon nanospheres wrapped with transition metal oxides nanostructures as non-precious catalysts for the electro-oxidation of hydrazine. *J. Electroanal. Chem.* **2020**, *873*, 114437. [\[CrossRef\]](#)
11. Chen, S.; Wang, C.; Liu, S.; Huang, M.; Lu, J.; Xu, P.; Tong, H.; Hu, L.; Chen, Q. Boosting hydrazine oxidation reaction on CoP/Co Mott-Schottky electrocatalyst through engineering active sites. *J. Phys. Chem. Lett.* **2021**, *12*, 4769–5044. [\[CrossRef\]](#) [\[PubMed\]](#)
12. Burshtein, T.Y.; Yasman, Y.; Muñoz-Moene, L.; Zagal, J.H.; Eisenberg, D. Hydrazine oxidation electrocatalysis. *ACS Catalysis* **2024**, *14*, 2264–2283. [\[CrossRef\]](#)
13. Dong, Q.; Li, Y.; Ji, S.; Wang, H.; Kan, Z.; Linkov, V.; Wang, R. Directional manipulation of electron transfer in copper/nitrogen doped carbon by Schottky barrier for efficient anodic hydrazine oxidation and cathodic oxygen reduction. *J. Colloid Interf. Sci.* **2023**, *652 Pt A*, 57–68. [\[CrossRef\]](#)

14. Zhang, C.M.; Zhou, B.; Gong, Y.; Shang, M.; Xiao, W.; Wang, J.; Dai, C.; Zhang, H.; Wu, Z.; Wang, L. Regulating Mo-based alloy-oxide active interfaces for efficient alkaline hydrogen evolution assisted by hydrazine oxidation. *J. Colloid Interf. Sci.* **2024**, *667*, 73–81. [\[CrossRef\]](#) [\[PubMed\]](#)
15. Askari, M.B.; Salarizadeh, P.; Beitollahi, H.; Tajik, S.; Eshghi, A.; Azizi, S. Electro-oxidation of hydrazine on NiFe<sub>2</sub>O<sub>4</sub>-rGO as a high-performance nano-electrocatalyst in alkaline media. *Mater. Chem. Phys.* **2022**, *275*, 125313. [\[CrossRef\]](#)
16. Zhang, Z.; Wen, H.; Liu, J.; Wang, P. Ni-W solid solution alloy as a high-performance catalyst for hydrazine oxidation. *Electrochim. Acta* **2023**, *471*, 143356. [\[CrossRef\]](#)
17. Gopi, S.; Yun, K. Synergistic sulfur-doped tri-metal phosphide electrocatalyst for efficient hydrazine oxidation in water electrolysis: Toward high-performance hydrogen fuel generation. *J. Alloys Compn.* **2024**, *986*, 174044. [\[CrossRef\]](#)
18. Wei, X.; Wang, T.; Dai, H.; Li, S. Multifold nanotwin-enhanced catalytic activity of Ni-Zn-Cu for hydrazine oxidation. *J. Alloys Compd.* **2024**, *997*, 174898. [\[CrossRef\]](#)
19. Zhao, Y.; Sun, Y.; Li, H.; Zeng, S.; Li, R.; Yao, Q.; Chen, H.; Zheng, Y.; Qu, K. Highly enhanced hydrazine oxidation on bifunctional Ni tailored by alloying for energy-efficient hydrogen production. *J. Colloid Interf. Sci.* **2023**, *652*, 1848–1856. [\[CrossRef\]](#)
20. Guo, R.; Zhang, Y.; Zhang, X.; Ma, M.; Hu, T. Enhanced catalytic oxidation of hydrazine of CoO/Co<sub>3</sub>O<sub>4</sub> heterojunction on N-doped carbon. *Electrochim. Acta* **2023**, *458*, 142537. [\[CrossRef\]](#)
21. Filanovsky, B.; Granot, E.; Presman, I.; Kuras, I.; Patolsky, F. Long-term room-temperature hydrazine/air fuel cells based on low-cost nanotextured Cu–Ni catalysts. *J. Power Sources* **2014**, *246*, 423–429. [\[CrossRef\]](#)
22. Liu, H.; Liu, Y.; Li, M.; Liu, X.; Luo, J. Transition-metal-based electrocatalysts for hydrazine-assisted hydrogen production. *Mater. Today Adv.* **2020**, *7*, 100083. [\[CrossRef\]](#)
23. Hu, X.; Wang, X.; Liu, T.; Liang, Z.; Zhang, X.; Tian, J. Fine-tuning catalytic performance of ultrafine bimetallic nickel-platinum on metal-organic framework derived nanoporous carbon/metal oxide toward hydrous hydrazine decomposition. *Int. J. Hydrogen Energy* **2023**, *48*, 16001–16006. [\[CrossRef\]](#)
24. Men, Y.; Su, J.; Wang, X.; Cai, P.; Cheng, G.; Luo, W. NiPt nanoparticles supported on CeO<sub>2</sub> nanospheres for efficient catalytic hydrogen generation from alkaline solution of hydrazine. *Chinese Chem. Lett.* **2019**, *30*, 634–637. [\[CrossRef\]](#)
25. Khan, S.; Shah, S.S.; Ahmad, A.; Yurtcan, A.B.; Jabeen, E.; Alshgari, R.A.; Janjua, N.K. Ruthenium and palladium oxide promoted zinc oxide nanoparticles: Efficient electrocatalysts for hydrazine oxidation reaction. *J. Electroanal. Chem.* **2022**, *917*, 116422. [\[CrossRef\]](#)
26. Hanindriyo, A.T.; Prawiraa, T.Y.Y.; Agustaa, M.K.; Maezonob, R.; Dipojono, H.K. Computational design of Ni-Zn based catalyst for direct hydrazine fuel cell catalyst using density functional theory. *Procedia Engineer.* **2017**, *170*, 148–153. [\[CrossRef\]](#)
27. Tamašauskaitė-Tamašiūnaitė, L.; Šimkūnaitė, D.; Nacys, A.; Balčiūnaitė, A.; Zabielaite, A.; Norkus, E. Chapter 11-Direct hydrazine fuel cells (DHFCs). In *Direct Liquid Fuel Cells Fundamentals, Advances and Future*; Academic Press: Cambridge, MA, USA, 2021; pp. 233–248.
28. Ma, J.; Choudhury, N.A.; Sahai, Y. A comprehensive review of direct borohydride fuel cells. *Renew. Sust. Energy Rev.* **2010**, *14*, 183–199. [\[CrossRef\]](#)
29. Abdolmaleki, M.; Ahadzadeh, I.; Goudarziafshar, H. Direct hydrazine-hydrogen peroxide fuel cell using carbon supported Co@Au core-shell nanocatalyst. *Int. J. Hydrogen Energy* **2017**, *42*, 15623–15631. [\[CrossRef\]](#)
30. Bedin, K.C.; Cazetta, A.L.; Souza, I.P.A.F.; Spessato, L.; Zhang, T.; Araújo, R.A.; Silva, R.; Asefa, T.; Almeida, V.C. N-doped spherical activated carbon from dye adsorption: Bifunctional electrocatalyst for hydrazine oxidation and oxygen reduction. *J. Environ. Chem. Engineer.* **2022**, *10*, 107458. [\[CrossRef\]](#)
31. Serov, A.; Kwak, C. Direct hydrazine fuel cells: A review. *App. Catal. B-Environ.* **2010**, *98*, 1–9. [\[CrossRef\]](#)
32. Vorms, E.A.; Papaefthymiou, V.; Faverge, T.; Bonnefont, A.; Chatenet, M.; Savinova, E.R.; Oshchepkov, A.G. Mechanism of the hydrazine hydrate electrooxidation reaction on metallic Ni electrodes in alkaline media as revealed by electrochemical methods, online DEMS and ex situ XPS. *Electrochim. Acta* **2024**, *507*, 145056. [\[CrossRef\]](#)
33. Sakamoto, T.; Asazawa, K.; Martinez, U.; Halevi, B.; Suzuki, T.; Arai, S.; Matsumura, D.; Nishihata, Y.; Atanassov, P.; Tanaka, H. Electrooxidation of hydrazine hydrate using Ni–La catalyst for anion exchange membrane fuel cells. *J. Power Sources* **2013**, *234*, 252–259. [\[CrossRef\]](#)
34. Ong, B.C.; Kamarudin, S.K.; Basri, S. Direct liquid fuel cells: A review. *Int. J. Hydrogen Energy* **2017**, *42*, 10142–10157. [\[CrossRef\]](#)
35. Dekel, D.R. Review of cell performance in anion exchange membrane fuel cells. *J. Power Sources* **2018**, *375*, 158–169. [\[CrossRef\]](#)
36. Hosseini, M.G.; Rashidi, N.; Mahmoodi, R.; Omer, M. Preparation of Pt/G and PtNi/G nanocatalysts with high electrocatalytic activity for borohydride oxidation and investigation of different operation condition on the performance of direct borohydride-hydrogen peroxide fuel cell. *Mater. Chem. Phys.* **2018**, *208*, 207–219. [\[CrossRef\]](#)
37. Oliveira, R.C.P.; Vasić, M.; Santos, D.M.F.; Babić, B.; Hercigonja, R.; Sequeira, C.A.C.; Šljukić, B. Performance assessment of a direct borohydride-peroxide fuel cell with Pd-impregnated faujasite X zeolite as anode electrocatalyst. *Electrochim. Acta* **2018**, *269*, 517–525. [\[CrossRef\]](#)



38. Mayuri, P.; Huang, S.-T.; Mani, V.; Kumar, A.S. A new organic redox species-indole tetraone trapped MWCNT modified electrode prepared by in-situ electrochemical oxidation of indole for a bifunctional electrocatalysis and simultaneous flow injection electroanalysis of hydrazine and hydrogen peroxide. *Electrochim. Acta* **2018**, *268*, 150–162. [CrossRef]
39. Li, M.; Li, N.; Shao, W.; Zhou, C. Synthesis of carbon nanofibers by CVD as a catalyst support material using atomically ordered Ni<sub>3</sub>C nanoparticles. *Nanotechnology* **2016**, *27*, 505706. [CrossRef]
40. Saconsint, S.; Sae-tang, N.; Srifa, A.; Koo-Amornpattana, W.; Assabumrungrat, S.; Fukuhara, C.; Ratchahat, S. Development of high-performance nickel-based catalysts for production of hydrogen and carbon nanotubes from biogas. *Sci. Rep.* **2022**, *12*, 15195. [CrossRef]
41. Bansal, R.C.; Goyal, M. *Activated Carbon Adsorption*; Taylor & Francis: Abingdon, UK, 2005.
42. Plavniece, A.; Volperts, A.; Dobeles, G.; Zhurins, A.; Kaare, K.; Kruusenberg, I.; Kaprans, K.; Knoks, A.; Kleperis, J. Wood and black liquor-based N-doped activated carbon for energy application. *Sustainability* **2021**, *13*, 9237. [CrossRef]
43. Cançado, L.G.; Jorio, A.; Ferreira, E.H.M.; Stavale, F.; Achete, C.A.; Capaz, R.B.; Moutinho, M.V.O.; Lombardo, A.; Kulmala, T.S.; Ferrari, A.C. Quantifying defects in graphene via Raman spectroscopy at different excitation energies. *Nano Lett.* **2011**, *11*, 3190–3196. [CrossRef] [PubMed]
44. Ribeiro-Soares, J.; Oliveros, M.E.; Garin, C.; David, M.V.; Martins, L.G.P.; Almeida, C.A.; Martins-Ferreira, E.H.; Takai, K.; Enoki, T.; Margalhões-Paniago, R.; et al. Structural analysis of polycrystalline graphene by Raman spectroscopy. *Carbon* **2015**, *95*, 646–652. [CrossRef]
45. Jorio, A.; Cançado, L.G. Perspectives on Raman spectroscopy of graphene-based systems: From the perfect two-dimensional surface to charcoal. *Phys. Chem. Chem. Phys.* **2012**, *14*, 15246–15256. [CrossRef]
46. Jorio, A.; Filho, A.G.S. Raman studies of carbon nanostructures. *Annu. Rev. Mater. Res.* **2016**, *46*, 357–382. [CrossRef]
47. Trusovas, R.; Ratautas, K.; Račiukaitis, G.; Niaura, G. Graphene layer formation in pinewood by nanosecond and picosecond laser. *Appl. Surf. Sci.* **2019**, *471*, 154–161. [CrossRef]
48. Biesinger, M.C. Accessing the robustness of adventitious carbon for charge referencing (correction) purposes in XPS analysis: Insights from a multi-user facility data review. *Appl. Surf. Sci.* **2022**, *597*, 153681. [CrossRef]
49. Baccile, N.; Laurent, G.; Babonneau, F.; Fayon, F.; Titirici, M.M.; Antonietti, M. Structural characterization of hydrothermal carbon spheres by advanced solid-state MAS <sup>13</sup>C NMR investigations. *J. Phys. Chem. C* **2009**, *113*, 9644–9654. [CrossRef]
50. Xue, Y.; Gao, B.; Yao, Y.; Inyang, M.; Zhang, M.; Zimmerman, A.R.; Ro, K.S. Hydrogen peroxide modification enhances the ability of biochar (hydrochar) produced from hydrothermal carbonization of peanut hull to remove aqueous heavy metals: Batch and column tests. *Chem. Eng. J.* **2012**, *200–202*, 673–680. [CrossRef]
51. Gonçalves, L.P.L.; Serov, A.; McCool, G.; Dicomie, M.; Sousa, J.P.S.; Soares, O.S.G.P.; Bondarchuk, O.; Petrovykh, D.Y.; Lebedev, O.I.; Pereira, M.F.R.; et al. New opportunity for carbon-supported Ni-based electrocatalysts: Gas-phase CO<sub>2</sub> methanation. *ChemCatChem* **2021**, *13*, 4770–4779. [CrossRef]
52. Biesinger, M.C.; Payne, B.P.; Lau, L.W.M.; Gerson, A.; Smart, R.S.C. X-ray photoelectron spectroscopy chemical state quantification of mixed nickel metal, oxide and hydroxide system. *Surf. Interf. Anal.* **2009**, *41*, 324–332. [CrossRef]
53. Biesinger, M.C.; Payne, B.P.; Grosvenor, A.P.; Lau, L.W.M.; Gerson, A.R.; Smart, R.S.C. Resolving surface chemical states in XPS analysis of first row transition metals, oxides and hydroxides: Cr, Mn, Fe, Co and Ni. *Appl. Surf. Sci.* **2011**, *257*, 2717–2730. [CrossRef]
54. Naumkin, A.V.; Kraut-Vass, A.; Gaarenstroom, S.W.; Powel, C.J. NIST X-Ray Photoelectron Spectroscopy Database (SRD 20), Version 5.0 (Web Version). 2023. Available online: <https://srdata.nist.gov/xps/> (accessed on 9 March 2025).
55. Wang, G.; Chen, J.; Cai, P.; Jia, J.; Wen, Z. A self-supported Ni–Co perselenide nanorod array as a high-activity bifunctional electrode for a hydrogen-producing hydrazine fuel cell. *J. Mater. Chem. A* **2018**, *6*, 17763–17770. [CrossRef]
56. Hosseini, M.G.; Daneshvari-Esfahlan, V.; Aghajani, H.; Wolf, S.; Hacker, V. Palladium-Nickel electrocatalysts on nitrogen-doped reduced graphene oxide nanosheets for direct hydrazine/hydrogen peroxide fuel cells. *Catalysts* **2021**, *11*, 1372. [CrossRef]
57. Crisafulli, R.; De Barros, V.V.S.; Rodrigues De Oliveira, F.E.; De Araújo Rocha, T.; Zignani, S.; Spadaro, L.; Palella, A.; Dias, J.A.; Linares, J.J. On the promotional effect of Cu on Pt for hydrazine electrooxidation in alkaline medium. *Appl. Catal. B Environ.* **2018**, *236*, 36–44. [CrossRef]
58. Feng, G.; Kuang, Y.; Li, P.; Han, N.; Sun, M.; Zhang, G.; Sun, X. Single crystalline ultrathin nickel–cobalt alloy nanosheets array for direct hydrazine fuel cells. *Adv. Sci.* **2017**, *4*, 1600179. [CrossRef]
59. Lei, Y.; Liu, Y.; Fan, B.; Mao, L.; Yu, D.; Huang, Y.; Guo, F. Facile fabrication of hierarchically porous Ni foam@ Ag-Ni catalyst for efficient hydrazine oxidation in alkaline medium. *J. Taiwan Inst. Chem. Eng.* **2019**, *105*, 75–84. [CrossRef]

**Disclaimer/Publisher’s Note:** The statements, opinions and data contained in all publications are solely those of the individual author(s) and contributor(s) and not of MDPI and/or the editor(s). MDPI and/or the editor(s) disclaim responsibility for any injury to people or property resulting from any ideas, methods, instructions or products referred to in the content.